

COMPUTATIONAL STUDY OF NON-NEWTONIAN EYRING-POWELL FLUID FROM A  
HORIZONTAL CIRCULAR CYLINDER WITH BIOT NUMBER EFFECTS

S. ABDUL GAFFAR<sup>1\*</sup>, V. RAMACHANDRA PRASAD<sup>2</sup>, E. KESHA REDDY<sup>1</sup>

<sup>1</sup>Department of Mathematics,  
Jawaharlal Nehru Technological University Anantapur, Anantapuram-515002, India.

<sup>2</sup>Department of Mathematics,  
Madanapalle Institute of Technology and Science, Madanapalle-517325, India.

(Received On: 12-08-15; Revised & Accepted On: 28-09-15)

---

ABSTRACT

*In this article, we investigate the nonlinear steady boundary layer flow and heat transfer of an incompressible Eyring-Powell non-Newtonian fluid from a Horizontal Circular Cylinder. The transformed conservation equations are solved numerically subject to physically appropriate boundary conditions using a second-order accurate implicit finite-difference Keller Box technique. The numerical code is validated with previous studies. The influence of a number of emerging non-dimensional parameters, namely the Eyring-Powell rheological fluid parameter ( $\varepsilon$ ), the local non-Newtonian parameter based on length scale ( $\delta$ ), Prandtl number ( $Pr$ ), Biot number ( $\gamma$ ) and dimensionless tangential coordinate ( $\xi$ ) on velocity and temperature evolution in the boundary layer regime are examined in detail. Furthermore the effects of these parameters on surface heat transfer rate and local skin friction are also investigated. Validation with earlier Newtonian studies is presented and excellent correlation achieved. It is found that the velocity and the Nusselt number (heat transfer rate) are reduced with increasing fluid parameter ( $\varepsilon$ ), whereas temperature and skin friction are enhanced. Increasing fluid parameter, the local non-Newtonian parameter based on length scale ( $\delta$ ) enhances the velocity, local skin friction and the Nusselt number (heat transfer rate) but reduces the temperature. An increase in the Biot number ( $\gamma$ ) is observed to enhance velocity, temperature, local skin friction and Nusselt number. An increasing Prandtl number,  $Pr$ , is found to decrease both velocity and temperature. The study is relevant to chemical materials processing applications.*

**Keywords:** Non-Newtonian Eyring-Powell model; Horizontal Cylinder; finite difference numerical method; heat transfer; boundary layers; skin friction; Nusselt number; Biot number.

---

NOMENCLATURE

$C_f$	skin friction coefficient
$C$	fluid parameter
$f$	non-dimensional stream function
$Gr$	Grashof number
$g$	acceleration due to gravity
$k$	thermal conductivity of fluid
$Nu$	local Nusselt number
$Pr$	Prandtl number
$T$	temperature of the fluid
$u, v$	non-dimensional velocity components along the x- and y- directions, respectively
$V$	velocity vector
$x$	stream wise coordinate
$y$	transverse coordinate

---

**Corresponding Author: S. Abdul Gaffar<sup>1\*</sup>, <sup>1</sup>Department of Mathematics,  
Jawaharlal Nehru Technological University Anantapur, Anantapuram-515002, India.**

### Greek

$\alpha$	thermal diffusivity
$\beta$	fluid parameter
$\phi$	non-dimensional concentration
$\eta$	dimensionless radial coordinate
$\mu$	dynamic viscosity
$\nu$	kinematic viscosity
$\theta$	dimensionless temperature
$\rho$	density of non-Newtonian fluid
$\xi$	dimensionless tangential coordinate
$\psi$	dimensionless stream function
$\varepsilon$	fluid parameter
$\gamma$	Biot number

### Subscripts

$w$	conditions at the wall (cylinder surface)
$\infty$	free stream conditions

## 1. INTRODUCTION

The dynamics of non-Newtonian fluids has been a popular area of research owing to ever-increasing applications in chemical and process engineering. Examples of such fluids include coal-oil slurries, shampoo, paints, clay coating and suspensions, grease, cosmetic products, custard, physiological liquids (blood, bile, synovial fluid) etc. The classical equations employed in simulating Newtonian viscous flows i.e. the Navier–Stokes equations fail to simulate a number of critical characteristics of non-Newtonian fluids. Hence several constitutive equations of non-Newtonian fluids have been presented over the past decades. The relationship between the shear stress and rate of strain in such fluids are very complicated in comparison to viscous fluids. The viscoelastic features in non-Newtonian fluids add more complexities in the resulting equations when compared with Navier–Stokes equations. Significant attention has been directed at mathematical and numerical simulation of non-Newtonian fluids. Recent investigations have implemented, respectively the Casson model [1], second-order Reiner-Rivlin differential fluid models [2], power-law nanoscale models [3], Eringen micro-morphic models [4] and Jefferys viscoelastic model [5].

Convective heat transfer has also mobilized substantial interest owing to its importance in industrial and environmental technologies including energy storage, gas turbines, nuclear plants, rocket propulsion, geothermal reservoirs, photovoltaic panels etc. The convective boundary condition has also attracted some interest and this usually is simulated via a Biot number in the wall thermal boundary condition. Recently, Ishak [6] discussed the similarity solutions for flow and heat transfer over a permeable surface with convective boundary condition. Aziz [7] provided a similarity solution for laminar thermal boundary layer over a flat surface with a convective surface boundary condition. Aziz [8] further studied hydrodynamic and thermal slip flow boundary layers with an iso-flux thermal boundary condition. The buoyancy effects on thermal boundary layer over a vertical plate subject a convective surface boundary condition was studied by Makinde and Olanrewaju [9]. Further recent analyses include Makinde and Aziz [10]. Gupta *et al.* [11] used a variational finite element to simulate mixed convective-radiative micropolar shrinking sheet flow with a convective boundary condition. Swapna *et al.* [12] studied convective wall heating effects on hydromagnetic flow of a micropolar fluid. Makinde *et al.* [13] studied cross diffusion effects and Biot number influence on hydromagnetic Newtonian boundary layer flow with homogenous chemical reactions and **MAPLE** quadrature routines. Bég *et al.* [14] analyzed Biot number and buoyancy effects on magnetohydrodynamic thermal slip flows. Subhashini *et al.* [15] studied wall transpiration and cross diffusion effects on free convection boundary layers with a convective boundary condition.

An interesting non-Newtonian model developed for chemical engineering systems is the *Eyring-Powell* fluid model. This rheological model has certain advantages over the other non-Newtonian formulations, including simplicity, ease of computation and physical robustness. Furthermore it is deduced from kinetic theory of liquids rather than the empirical relation. Additionally it correctly reduces to Newtonian behavior for low and high shear rates [16]. Several communications utilizing the Eyring–Powell fluid model have been presented in the scientific literature. Zueco and Bég [17] numerically studied the pulsatile flow of Eyring–Powell model using the network electro-thermal solver code, **PSPICE**. Islam *et al.* [18] derived Homotopy perturbation solutions for slider bearings lubricated with Eyring-Powell fluids. Patel and Timol [19] numerically examined the flow of Eyring–Powell fluids from a two-dimensional wedge. Further investigations implementing the Eyring-Powell model in transport phenomena include Sirohi *et al.* [20] for wedge flows, Akbar *et al.* [21] for peristaltic thermal convection flows of reactive biofluids, Hayat *et al.* [22] for Sakiadis flows, Etchart [23] for entry length pipe flows and Hassanien and Hady [24] for magneto-convective flows.

Sirohiet *et al.* [25] used orthogonal collocation, asymptotic and transformation methods to simulate Eyring-Powell flow from an accelerated sheet. The Eyring-Powell model was also deployed by Yürüsöy [26] to investigate bearing tribological flows, by Ai and Vafai [27] to simulate Stokesian impulsively-started plate flows and also by Adesanya and Gbadeyan [28] for channel flows.

In many chemical engineering and nuclear process systems, *curvature of the vessels employed* is a critical aspect of optimizing thermal performance. Examples of curved bodies featuring in process systems include torus geometries, wavy surfaces, cylinders, cones, ellipses, oblate spheroids and in particular, spherical geometries. A number of theoretical and computational studies have been communicated on transport phenomena from cylindrical bodies, which frequently arise in polymer processing systems. These Newtonian studies were focused more on heat transfer aspects and include Eswara and Nath [29], Rotte and Beek [30] and the pioneering analysis of Sakiadis [31]. Further more recent studies examining multi-physical and chemical transport from cylindrical bodies include Zueco *et al.* [32, 33]. An early investigation of rheological boundary layer heat transfer from a horizontal cylinder was presented by Chen and Leonard [34] who considered the power-law model and demonstrated that the transverse curvature has a strong effect on skin friction at moderate and large distances from the leading edge of the boundary layer. Lin and Chen [35] also studied axisymmetric laminar boundary-layer convection flow of a power-law non-Newtonian fluid over both a circular cylinder and a spherical body using the Merk-Chao series solution method. Pop *et al.* [36] simulated numerically the steady laminar forced convection boundary layer of power-law non-Newtonian fluids on a continuously moving cylinder with the surface maintained at a uniform temperature or uniform heat flux. Further non-Newtonian models employed in analyzing convection flows from cylinders include micropolar liquids [37], viscoelastic materials [38, 39], micropolar nanofluids [40] and Casson fluids [41].

The objective of the present study is to investigate the laminar boundary layer flow and heat transfer of an *Eyring-Powell* non-Newtonian fluid from a horizontal circular cylinder. The non-dimensional equations with associated dimensionless boundary conditions constitute a highly nonlinear, coupled two-point boundary value problem. Keller's implicit finite difference "box" scheme is implemented to solve the problem [42]. The effects of the emerging thermophysical parameters, namely *the rheological parameters* ( $\epsilon, \delta$ ), *Biot number* ( $\gamma$ ) and *Prandtl number* ( $Pr$ ), on the velocity, temperature, local skin friction, and heat transfer rate (local Nusselt number) characteristics are studied. The present problem has to the authors' knowledge not appeared thus far in the scientific literature and is relevant to polymeric manufacturing processes in chemical engineering.

## 2. NON-NEWTONIAN CONSTITUIVE EYRING-POWELL FLUID MODEL

In the present study a subclass of non-Newtonian fluids known as the *Eyring-Powell fluid* is employed owing to its simplicity. The Cauchy stress tensor, in an Eyring-Powell non-Newtonian fluid [16] takes the form:

$$\tau_{ij} = \mu \frac{\partial u_i}{\partial x_j} + \frac{1}{\beta} \sinh^{-1} \left( \frac{1}{C} \frac{\partial u_i}{\partial x_j} \right) \quad (1)$$

where  $\mu$  is dynamic viscosity,  $\beta$  and  $C$  are the rheological fluid parameters of the Eyring-Powell fluid model. Considering the second-order approximation of the  $\sinh^{-1}$  function as:

$$\sinh^{-1} \left( \frac{1}{C} \frac{\partial u_i}{\partial x_j} \right) \cong \frac{1}{C} \frac{\partial u_i}{\partial x_j} - \frac{1}{6} \left( \frac{1}{C} \frac{\partial u_i}{\partial x_j} \right)^3, \quad \left| \frac{1}{C} \frac{\partial u_i}{\partial x_j} \right| \ll 1, \quad (2)$$

The introduction of the appropriate terms into the flow model is considered next. The resulting boundary value problem is found to be well-posed and permits an excellent mechanism for the assessment of rheological characteristics on the flow behaviour.

## 3. MATHEMATICAL FLOW MODEL

Steady, double-diffusive, laminar, incompressible flow of an Eyring-Powell fluid from a horizontal cylinder, is considered, as illustrated in **Figure 1**. The  $x$ -coordinate (tangential) is measured along the circumference of the horizontal cylinder from the lowest point and the  $y$ -coordinate (radial) is directed perpendicular to the surface, with  $a$  denoting the radius of the horizontal cylinder.  $\Phi = x/a$  is the angle of the  $y$ -axis with respect to the vertical ( $0 \leq \Phi \leq \pi$ ). The gravitational acceleration  $g$ , acts downwards. We also assume that the Boussineq approximation holds i.e. that density variation is only experienced in the buoyancy term in the momentum equation.

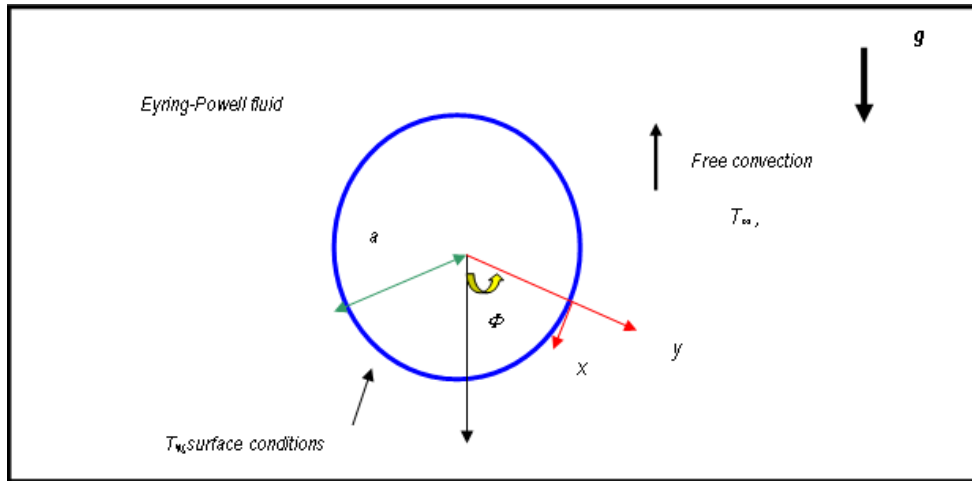


Figure 1: Physical model and coordinate system

Both horizontal cylinder and Eyring-Powell fluid are maintained initially at the same temperature. Instantaneously they are raised to a temperature  $T_w > T_\infty$ , the ambient temperature of the fluid which remains unchanged. In line with the approach of Yih [43] and introducing the boundary layer approximations, the equations for *mass, momentum, and energy*, can be written as follows:

$$\frac{\partial u}{\partial x} + \frac{\partial v}{\partial y} = 0 \quad (3)$$

$$u \frac{\partial u}{\partial x} + v \frac{\partial u}{\partial y} = \left( \nu + \frac{1}{\rho \beta C} \right) \frac{\partial^2 u}{\partial y^2} - \frac{1}{2 \rho \beta C^3} \left( \frac{\partial u}{\partial y} \right)^2 \frac{\partial^2 u}{\partial y^2} + g \beta_1 \sin \left( \frac{x}{a} \right) (T - T_\infty) \quad (4)$$

$$u \frac{\partial T}{\partial x} + v \frac{\partial T}{\partial y} = \alpha \frac{\partial^2 T}{\partial y^2} \quad (5)$$

Where  $u$  and  $v$  are the velocity components in the  $x$  - and  $y$  - directions respectively,  $\nu = \frac{\mu}{\rho}$  is the kinematic viscosity

of the Eyring-Powell fluid,  $\beta_1$  is the coefficient of thermal expansion. The Eyring-Powell fluid model therefore introduces a *mixed* derivative (second order, second degree) into the momentum boundary layer equation (4). The non-Newtonian effects feature in the shear terms only of eqn. (4) and not the convective (acceleration) terms. The third term on the right hand side of eqn. (4) represents the *thermal buoyancy force* and couples the velocity field with the temperature field equation (5)

$$\text{At } y = 0, \quad u = 0, \quad v = 0, \quad -k \frac{\partial T}{\partial y} = h_w (T_w - T)$$

$$\text{As } y \rightarrow \infty, \quad u \rightarrow 0, \quad T \rightarrow T_\infty \quad (6)$$

Here  $T_\infty$  is the free stream temperature,  $h_w$  is the convective heat transfer coefficient,  $T_w$  is the convective fluid temperature.

The stream function  $\psi$  is defined by  $u = \frac{\partial \psi}{\partial y}$  and  $v = -\frac{\partial \psi}{\partial x}$ , and therefore, the continuity equation is automatically

satisfied. In order to render the governing equations and the boundary conditions in dimensionless form, the following non-dimensional quantities are introduced.

$$\xi = \frac{x}{a}, \quad \eta = \frac{y}{a} Gr^{1/4}, \quad f = \frac{\psi}{\nu \xi} Gr^{-1/4}, \quad \theta(\xi, \eta) = \frac{T - T_\infty}{T_w - T_\infty}, \quad \text{Pr} = \frac{\nu}{\alpha},$$

$$Gr = \frac{g \beta_1 (T_w - T_\infty) a^3}{\nu^2}, \quad \varepsilon = \frac{1}{\mu \beta C}, \quad \delta = \frac{\nu^2}{2 C^2 a^4} Gr^{3/2} \quad (7)$$

All terms are defined in the nomenclature. In view of the transformation defined in eqn. (7), the boundary layer eqns. (4)-(6) are reduced to the following coupled, nonlinear, dimensionless partial differential equations for momentum and energy for the regime:

$$(1 + \varepsilon) f''' + ff'' - (f')^2 - \varepsilon \delta \xi^2 (f'')^2 f''' + \theta \frac{\sin \xi}{\xi} = \xi \left( f' \frac{\partial f'}{\partial \xi} - f'' \frac{\partial f}{\partial \xi} \right) \quad (8)$$

$$\frac{\theta''}{Pr} + f\theta' = \xi \left( f' \frac{\partial \theta}{\partial \xi} - \theta' \frac{\partial f}{\partial \xi} \right) \quad (9)$$

The transformed dimensionless boundary conditions are:

$$\begin{aligned} \text{At } \eta = 0, \quad f = 0, \quad f' = 0, \quad \theta = 1 + \frac{\theta'}{\gamma} \\ \text{As } \eta \rightarrow \infty, \quad f' \rightarrow 0, \quad \theta \rightarrow 0 \end{aligned} \quad (10)$$

Here primes denote the differentiation with respect to  $\eta$  and  $\gamma = \frac{ah_w}{k} Gr^{-1/4}$  is the Biot number. The wall thermal boundary condition in (10) corresponds to convective cooling. The skin-friction coefficient (shear stress at the cylinder surface) and Nusselt number (heat transfer rate) can be defined using the transformations described above with the following expressions.

$$Gr^{-3/4} C_f = (1 + \varepsilon) \xi f''(\xi, 0) - \frac{\delta}{3} \varepsilon \xi^3 (f''(\xi, 0))^3 \quad (11)$$

$$Gr^{-1/4} Nu = -\theta'(\xi, 0) \quad (12)$$

The location,  $\xi \sim 0$ , corresponds to the vicinity of the lower stagnation point on the cylinder. Since  $\frac{\sin \xi}{\xi} \rightarrow 0/0$  i.e. 1.

For this scenario, the model defined by eqns. (8) to (9) contracts to an ordinary differential boundary value problem:

$$(1 + \varepsilon) f''' + ff'' - (f')^2 + \theta = 0 \quad (13)$$

$$\frac{1}{Pr} \theta'' + f\theta' = 0 \quad (14)$$

The general model is solved using a powerful and unconditionally stable finite difference technique introduced by Keller [44]. The Keller-box method has a second order accuracy with arbitrary spacing and attractive extrapolation features.

#### 4. NUMERICAL SOLUTION WITH KELLER BOX IMPLICIT METHOD

The Keller-Box implicit difference method is implemented to solve the nonlinear boundary value problem defined by eqns. (8)–(9) with boundary conditions (10). This technique, despite recent developments in other numerical methods, remains a powerful and very accurate approach for parabolic boundary layer flows. It is unconditionally stable and achieves exceptional accuracy [44]. Recently this method has been deployed in resolving many challenging, multi-physical fluid dynamics problems. These include hydromagnetic Sakiadisflow of non-Newtonian fluids [45], nanofluid transport from a stretching sheet [46], radiative rheological magnetic heat transfer [47], waterhammer modelling [48], porous media convection [49] and magnetized viscoelastic stagnation flows [50]. The Keller-Box discretization is *fully coupled* at each step which reflects the physics of parabolic systems – which are also fully coupled. Discrete calculus associated with the Keller-Box scheme has also been shown to be fundamentally different from all other mimetic (physics capturing) numerical methods, as elaborated by Keller [44]. The Keller Box Scheme comprises four stages.

- 1) Decomposition of the  $N^{\text{th}}$  order partial differential equation system to  $N$  first order equations.
- 2) Finite Difference Discretization.
- 3) Quasilinearization of Non-Linear Keller Algebraic Equations and finally.
- 4) Block-tridiagonal Elimination solution of the Linearized Keller Algebraic Equations

**Stage 1: Decomposition of N<sup>th</sup> order partial differential equation system to N first order equations**

Equations (8) – (9) subject to the boundary conditions (10) are first cast as a multiple system of first order differential equations. New dependent variables are introduced:

$$u(x, y) = f', v(x, y) = f'', s(x, y) = \theta, t(x, y) = \theta' \tag{15}$$

These denote the variables for velocity, temperature and concentration respectively. Now Equations (8) – (9) are solved as a set of fifth order simultaneous differential equations:

$$f' = u \tag{16}$$

$$u' = v \tag{17}$$

$$\theta' = t \tag{18}$$

$$(1 + \varepsilon)v' + fv - u^2 - \varepsilon\delta\xi^2 v^2 v' + s \frac{\sin \xi}{\xi} = \xi \left( u \frac{\partial u}{\partial \xi} - v \frac{\partial f}{\partial \xi} \right) \tag{19}$$

$$\frac{t'}{\text{Pr}} + ft = \xi \left( u \frac{\partial s}{\partial \xi} - t \frac{\partial f}{\partial \xi} \right) \tag{20}$$

Where primes denote differentiation with respect to the variable,  $\eta$ . In terms of the dependent variables, the boundary conditions assume the form:

$$\text{At } \eta = 0, \quad f = 0, \quad f' = 0, \quad \theta = 1 + \frac{\theta'}{\gamma} \tag{21}$$

$$\text{As } \eta \rightarrow \infty, \quad f' \rightarrow 0, \quad \theta \rightarrow 0 \tag{22}$$

**Stage 2: Finite Difference Discretization**

A two dimensional computational grid is imposed on the  $\xi$ - $\eta$  plane as depicted in Fig.2. The stepping process is defined by:

$$\eta_0 = 0, \quad \eta_j = \eta_{j-1} + h_j, \quad j = 1, 2, \dots, J, \quad \eta_J \equiv \eta_\infty \tag{23}$$

$$\xi^0 = 0, \quad \xi^n = \xi^{n-1} + k_n, \quad n = 1, 2, \dots, N \tag{24}$$

Where  $k_n$  is the  $\Delta\xi$  – spacing and  $h_j$  is the  $\Delta\eta$  – spacing.

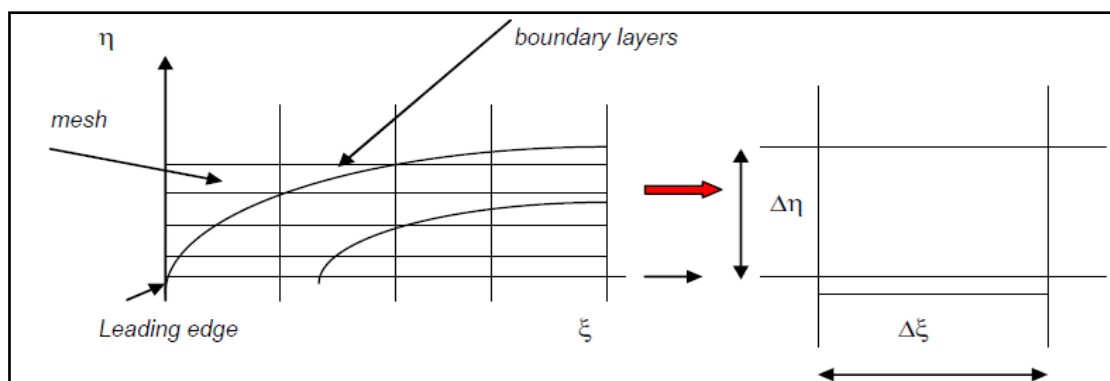


**Figure 2:** Keller box computational domain

If  $g^n$  denotes the value of any variable at  $(\eta_j, \xi^n)$ , then the variables and derivatives of Equations (16) – (20) at  $(\eta_{j-1/2}, \xi^{n-1/2})$  are replaced by:

$$g_{j-1/2}^{n-1/2} = \frac{1}{4} (g_j^n + g_{j-1}^n + g_j^{n-1} + g_{j-1}^{n-1}), \tag{25}$$

$$\left( \frac{\partial g}{\partial \eta} \right)_{j-1/2}^{n-1/2} = \frac{1}{2h_j} (g_j^n - g_{j-1}^n + g_j^{n-1} - g_{j-1}^{n-1}), \tag{26}$$

$$\left( \frac{\partial g}{\partial \xi} \right)_{j-1/2}^{n-1/2} = \frac{1}{2k^n} (g_j^n - g_{j-1}^n + g_j^{n-1} - g_{j-1}^{n-1}), \tag{27}$$

The finite-difference approximation of eqns, (16) – (20) for the mid-point  $(\eta_{j-1/2}, \xi^n)$ , are:

$$h_j^{-1} (f_j^n - f_{j-1}^n) = u_{j-1/2}^n, \quad (28)$$

$$h_j^{-1} (u_j^n - u_{j-1}^n) = v_{j-1/2}^n, \quad (29)$$

$$h_j^{-1} (s_j^n - s_{j-1}^n) = t_{j-1/2}^n, \quad (30)$$

$$(1 + \varepsilon)(v_j - v_{j-1}) + (1 + \alpha) \frac{h_j}{4} (f_j + f_{j-1})(v_j + v_{j-1}) - (1 + \alpha) \frac{h_j}{4} (u_j + u_{j-1})^2 + \frac{Bh_j}{2} (s_j + s_{j-1}) - \xi^2 \frac{\varepsilon\delta}{4} (v_j + v_{j-1})^2 (v_j - v_{j-1}) + \frac{\alpha h_j}{2} v_{j-1}^{n-1} (f_j + f_{j-1}) - \frac{\alpha h_j}{2} f_{j-1}^{n-1} (v_j + v_{j-1}) = [R_1]_{j-1/2}^{n-1} \quad (31)$$

$$\frac{1}{Pr} (t_j - t_{j-1}) + (1 + \alpha) \frac{h_j}{4} (f_j + f_{j-1})(t_j + t_{j-1}) - \frac{\alpha h_j}{4} (u_j + u_{j-1})(s_j + s_{j-1}) + \frac{\alpha h_j}{2} s_{j-1}^{n-1} (u_j + u_{j-1}) - \frac{\alpha h_j}{2} u_{j-1/2}^{n-1} (s_j + s_{j-1}) - \frac{\alpha h_j}{2} f_{j-1/2}^{n-1} (t_j + t_{j-1}) + \frac{\alpha h_j}{2} t_{j-1/2}^{n-1} (f_j + f_{j-1}) = [R_2]_{j-1/2}^{n-1} \quad (32)$$

Where we have used the abbreviations

$$\alpha = \frac{\xi^{n-1/2}}{k_n}, \quad B = \frac{\sin(\xi^{n-1/2})}{\xi^{n-1/2}} \quad (33)$$

$$[R_1]_{j-1/2}^{n-1} = -h_j \left[ \begin{aligned} & (1 + \varepsilon)(v')_{j-1/2}^{n-1} + (1 - \alpha) f_{j-1/2}^{n-1} v_{j-1/2}^{n-1} - (1 - \alpha)(u_{j-1/2}^{n-1})^2 \\ & + B s_{j-1/2}^{n-1} - \varepsilon\delta\xi^2 (v^2)_{j-1/2}^{n-1} (v')_{j-1/2}^{n-1} \end{aligned} \right] \quad (34)$$

$$[R_2]_{j-1/2}^{n-1} = -h_j \left[ \frac{1}{Pr} (t')_{j-1/2}^{n-1} + (1 - \alpha) f_{j-1/2}^{n-1} t_{j-1/2}^{n-1} + \alpha u_{j-1/2}^{n-1} s_{j-1/2}^{n-1} \right] \quad (35)$$

The boundary conditions are:

$$f_0^n = u_0^n = 0, \quad s_0^n = 1, \quad u_J^n = 0, \quad v_J^n = 0, \quad s_J^n = 0 \quad (36)$$

### Stage 3: Quasilinearization of Non-Linear Keller Algebraic Equations

Assuming  $f_j^{n-1}, u_j^{n-1}, v_j^{n-1}, s_j^{n-1}, t_j^{n-1}$  to be known for  $0 \leq j \leq J$ , then Eqns. (28) – (32) constitute a system of  $5J+5$  equations for the solution of  $5J+5$  unknowns  $f_j^n, u_j^n, v_j^n, s_j^n, t_j^n, j = 0, 1, 2, \dots, J$ . This *non-linear* system of algebraic equations is *linearized* by means of Newton's method as explained in [42, 44].

### Stage 4: Block-tridiagonal Elimination Solution of Linear Keller Algebraic Equations

The linearized system is solved by the *block-elimination* method, since it possesses a block-tridiagonal structure. The block-tridiagonal structure generated consists of *block matrices*. The complete linearized system is formulated as a *block matrix system*, where each element in the coefficient matrix is a matrix itself, and this system is solved using the efficient Keller-box method. The numerical results are strongly influenced by the number of mesh points in both directions. After some trials in the  $\eta$ -direction (radial coordinate) a larger number of mesh points are selected whereas in the  $\xi$  direction (tangential coordinate) significantly less mesh points are utilized.  $\eta_{\max}$  has been set at 25 and this defines an adequately large value at which the prescribed boundary conditions are satisfied.  $\xi_{\max}$  is set at 3.0 for this flow domain. Mesh independence is achieved in the present computations. The numerical algorithm is executed in

**MATLAB** on a PC. The method demonstrates excellent stability, convergence and consistency, as elaborated by Keller [44].

## 5. NUMERICAL RESULTS AND INTERPRETATION

Comprehensive solutions have been obtained and are presented in **Tables 1-5** and **Figs. 3 - 10**. The numerical problem comprises two independent variables  $(\xi, \eta)$ , two dependent fluid dynamic variables  $(f, \theta)$  and five thermo-physical and body force control parameters, namely,  $\gamma, \delta, \varepsilon, Pr, \xi$ . The following default parameter values i.e.  $\gamma = 0.2, \delta = 0.1,$

$\varepsilon = 0.1$ ,  $Pr = 7.0$ ,  $\xi = 1.0$  are prescribed (unless otherwise stated). Furthermore the influence of stream-wise (transverse) coordinate on heat transfer characteristics is also investigated.

In Tables 1 & 2, we present the influence of the Eyring-Powell fluid parameter,  $\varepsilon$ , on the skin friction and heat transfer rate, along with a variation in Prandtl number ( $Pr$ ). With increasing  $\varepsilon$ , the skin friction is enhanced. The parameter  $\varepsilon$  is inversely proportional to the dynamic viscosity of the non-Newtonian fluid. There as  $\varepsilon$  is elevated, viscosity will be reduced and this will induce lower resistance to the flow at the surface of the cylinder i.e. accelerate the flow leading to an escalation of shear stress. Furthermore this trend is sustained at any Prandtl number. However an increase in Prandtl number markedly reduces the shear stress magnitudes. Similarly increasing  $\varepsilon$ , is observed to reduce heat transfer rates, again at all Prandtl numbers, whereas it strongly accentuates heat transfer rates. Magnitudes of shear stress are always positive indicating that flow reversal (backflow) never arises.

Tables 3 & 4 document results for the influence of the local non-Newtonian parameter (based on length scale  $x$ ) i.e.  $\delta$  and also the Prandtl number ( $Pr$ ) on skin friction and heat transfer rate. Skin friction is generally decreased with increasing  $\delta$ . However heat transfer rate (i.e. local Nusselt number function) is found to be enhanced with increasing  $\delta$ .

$\delta = \frac{v^2}{2C^2 a^4} Gr^{3/2}$  and inspection of this definition shows that the direct proportionality of  $\delta$  to kinematic viscosity ( $\nu$ ) (with all other parameters being maintained constant) will generate a strong resistance to the flow leading to a deceleration i.e. drop in shear stresses. Conversely the direct proportionality of  $\delta$  to Grashof number ( $Gr$ ) will imply that thermal buoyancy forces are enhanced as  $\delta$  increases and this will cause a boost in heat transfer by convection from the cylinder surface manifesting with the greater heat transfer rates observed in Tables 3 and 4. These tables also show that with an increase in the Prandtl number,  $Pr$ , the skin friction is also depressed whereas the heat transfer rate is elevated.

Table 5 presents the Keller box numerical values of the missing condition  $f''(\xi, 0)$  (in brackets) and skin friction  $C_f$  for various values of  $\delta$  and  $\varepsilon$ . It is found that skin friction is reduced with increasing values of  $\delta$ . Furthermore, the skin friction  $C_f$  is observed to be increased with a rise in the Eyring-Powell fluid parameter ( $\varepsilon$ ) for all values of the local non-Newtonian parameter ( $\delta$ ).

Figures 3(a) - 3(b) illustrates the effect of Eyring-Powell fluid parameter  $\varepsilon$ , on the velocity ( $f'$ ) and temperature ( $\theta$ ) distributions through the boundary layer regime. Velocity is significantly decreased with increasing  $\varepsilon$  at larger distance from the cylinder surface owing to the simultaneous drop in dynamic viscosity. Conversely temperature is consistently enhanced with increasing values of  $\varepsilon$ . The mathematical model reduces to the Newtonian viscous flow model as  $\varepsilon \rightarrow 0$  and  $\delta \rightarrow 0$ . The momentum boundary layer equation in this case contracts to the familiar equation for Newtonian

mixed convection from a plate, viz  $f''' + (1 + \xi \cot \xi) f f'' - f'^2 + \theta \frac{\sin \xi}{\xi} = \xi \left( f' \frac{\partial f'}{\partial \xi} - f'' \frac{\partial f}{\partial \xi} \right)$ . The thermal

boundary layer equation (9) remains unchanged. In fig. 3b temperatures are clearly minimized for the Newtonian case ( $\varepsilon=0$ ) and maximized for the strongest non-Newtonian case ( $\varepsilon=1.5$ ).

Figures 4(a) - 4(b) depict the velocity ( $f'$ ) and temperature ( $\theta$ ) distributions with increasing local non-Newtonian parameter,  $\delta$ . Very little tangible effect is observed in fig. 4a, although there is a very slight increase in velocity with increase in  $\delta$ . Similarly there is only a very slight depression in temperature magnitudes in Fig. 4(b) with a rise in  $\delta$ .

Figures 5(a) - 5(b) depict the evolution of velocity ( $f'$ ) and temperature ( $\theta$ ) functions with a variation in Biot number,  $\gamma$ . Dimensionless velocity component (fig. 5a) is considerably enhanced with increasing  $\gamma$ . In fig. 5b, an increase in Biot number is seen to considerably enhance temperatures throughout the boundary layer regime. For  $\gamma < 1$  i.e. small Biot numbers, the regime is frequently designated as being "thermally simple" and there is a presence of more

uniform temperature fields inside the boundary layer and the cylinder solid surface. For  $\gamma > 1$  thermal fields are anticipated to be non-uniform within the solid body. The Biot number effectively furnishes a mechanism for comparing the conduction resistance within a solid body to the convection resistance external to that body (offered by the surrounding fluid) for heat transfer. We also note that a Biot number in excess of 0.1, as studied in figs. 5a,b corresponds to a "thermally thick" substance whereas Biot number less than 0.1 implies a "thermally thin" material. Since  $\gamma$  is inversely proportional to thermal conductivity ( $k$ ), as  $\gamma$  increases, thermal conductivity will be reduced at the



cylinder surface and this will lead to a decrease in the rate of heat transfer from the boundary layer to within the cylinder, manifesting in a rise in temperature at the cylinder surface and in the body of the fluid- the maximum effect will be sustained at the surface, as witnessed in fig. 5b. However for a fixed wall convection coefficient and thermal conductivity, Biot number as defined in  $\gamma = \frac{xh_w}{k} Gr^{-1/4}$  is also directly inversely proportional to the local Grashof (free convection) number. As local Grashof number increases generally the enhancement in buoyancy causes a deceleration in boundary layer flows [51-53]; however as Biot number increases, the local Grashof number must decrease and this will induce the opposite effect i.e. accelerate the boundary layer flow, as shown in fig. 5a.

**Figures 6(a) – 6(b)** depicts the profiles for velocity ( $f'$ ) and temperature ( $\theta$ ) for various values of Prandtl number, Pr. It is observed that an increase in the Prandtl number significantly decelerates the flow i.e., velocity decreases. Also increasing Prandtl number is found to decelerate the temperature.

**Figures 7(a) – 7(b)** depict the velocity ( $f'$ ) and temperature ( $\theta$ ) distributions with dimensionless radial coordinate, for various transverse (stream wise) coordinate values,  $\xi$ . Generally velocity is noticeably lowered with increasing migration from the leading edge i.e. larger  $\xi$  values (figure 7a). The maximum velocity is computed at the lower stagnation point ( $\xi=0$ ) for low values of radial coordinate ( $\eta$ ). The transverse coordinate clearly exerts a significant influence on momentum development. A very strong increase in temperature ( $\theta$ ), as observed in figure 7b, is generated throughout the boundary layer with increasing  $\xi$  values. The temperature field decays monotonically. Temperature is maximized at the surface of the spherical body ( $\eta=0$ , for all  $\xi$ ) and minimized in the free stream ( $\eta=25$ ). Although the behaviour at the upper stagnation point ( $\xi=\pi$ ) is not computed, the pattern in figure 6b suggests that temperature will continue to progressively grow here compared with previous locations on the cylinder surface (lower values of  $\xi$ ).

**Figures 8(a) - 8(b)** show the influence of Eyring-Powell fluid parameter,  $\varepsilon$  on dimensionless skin friction coefficient  $\left( (1 + \varepsilon) \xi f''(\xi, 0) - \frac{\delta}{3} \varepsilon \xi^3 (f'''(\xi, 0))^3 \right)$  and heat transfer rate ( $\theta'(\xi, 0)$ ) at the cylinder surface. It is observed that the dimensionless skin friction is increased with the increase in  $\varepsilon$  i.e. the boundary layer flow is accelerated with decreasing viscosity effects in the non-Newtonian regime. Conversely the surface heat transfer rate is substantially decreased with increasing  $\varepsilon$  values. Decreasing viscosity of the fluid (induced by increasing the  $\varepsilon$  value) reduces thermal diffusion as compared with momentum diffusion. A decrease in heat transfer rate at the wall will imply less heat is convected from the fluid regime to the cylinder, thereby heating the boundary layer and enhancing temperatures.

**Figures 9(a) - 9(b)** illustrates the influence of the local non-Newtonian parameter,  $\delta$ , on the dimensionless skin friction coefficient and heat transfer rate. The skin friction (fig. 9a) at the cylinder surface is accentuated with increasing  $\delta$ , however only for very large values of the transverse coordinate,  $\xi$ . The flow is therefore strongly accelerated along the curved cylinder surface far from the lower stagnation point. Heat transfer rate (local Nusselt number) is enhanced with increasing  $\delta$ , again at large values of  $\xi$ , as computed in fig.9b.

**Figures 10 (a) - 10(b)** presents the influence of the Biot number,  $\gamma$ , on the dimensionless skin friction coefficient and heat transfer rate at the cylinder surface. The skin friction at the cylinder surface is found to be greatly increased with rising Biot number,  $\gamma$ . This is principally attributable to the decrease in Grashof (free convection) number which results in an acceleration in the boundary layer flow, as elaborated by Chen and Chen [53]. Heat transfer rate (local Nusselt number) is enhanced with increasing  $\gamma$ , at large values of  $\xi$ , as computed in fig.10(b).

## 6. CONCLUSIONS

Numerical solutions have been presented for the buoyancy-driven flow and heat transfer of Eyring-Powell flow external to a horizontal cylinder. The Keller-box implicit second order accurate finite difference numerical scheme has been utilized to efficiently solve the transformed, dimensionless velocity and thermal boundary layer equations, subject to realistic boundary conditions. Excellent correlation with previous studies has been demonstrated (see Appendix) testifying to the validity of the present code. The computations have shown that:

- (I) Increasing Eyring-Powell fluid parameter,  $\varepsilon$ , reduces the velocity and skin friction (surface shear stress) and heat transfer rate, whereas it elevates temperatures in the boundary layer.
- (II) Increasing local non-Newtonian parameter,  $\delta$ , increases the velocity, skin friction and Nusselt number for all values of radial coordinate i.e., throughout the boundary layer regime whereas it depresses temperature.
- (III) Increasing Biot number,  $\gamma$ , increases velocity, temperature and skin friction (surface shear stress).
- (IV) Increasing Prandtl number, Pr, decreases velocity and temperature.

- (V) Increasing transverse coordinate ( $\zeta$ ) generally decelerates the flow near the cylinder surface and reduces momentum boundary layer thickness whereas it enhances temperature and therefore increases thermal boundary layer thickness in Eyring-Powell non-Newtonian fluids.

Generally very stable and accurate solutions are obtained with the present finite difference code. The numerical code is able to solve nonlinear boundary layer equations very efficiently and therefore shows excellent promise in simulating transport phenomena in other non-Newtonian fluids. It is therefore presently being employed to study micropolar fluids [11, 12] and viscoplastic fluids [54] which also simulate accurately many chemical engineering working fluids in curved geometrical systems.

## 7. REFERENCES

1. V. Ramachandra Prasad, A SubbaRao, N Bhaskar Reddy, B Vasu and O Anwar Bég, Modelling laminar transport phenomena in a Casson rheological fluid from a horizontal circular cylinder with partial slip, *ProcIMechE Part E: J Process Mechanical Engineering* (2013). DOI: 10.1177/0954408912466350.
2. M. Norouzi, M. Davoodi, O. Anwar Bég and A.A. Joneidi, Analysis of the effect of normal stress differences on heat transfer in creeping viscoelastic Dean flow, *Int. J. Thermal Sciences* 69, 61-69 (2013).
3. M. J. Uddin, N. H. M. Yusoff, O. Anwar Bég and A. I. Ismail, Lie group analysis and numerical solutions for non-Newtonian nanofluid flow in a porous medium with internal heat generation, *PhysicaScripta*, 87 (14pp) (2013).
4. M.M. Rashidi, M. Keimanesh, O. Anwar Bég, T.K. Hung, Magneto-hydrodynamic biorheological transport phenomena in a porous medium: A simulation of magnetic blood flow control, *Int. J. Numer. Meth. Biomed. Eng.* 27, 805-821 (2011).
5. D. Tripathi, S.K. Pandey and O. Anwar Bég, Mathematical modelling of heat transfer effects on swallowing dynamics of viscoelastic food bolus through the human oesophagus, *Int. J. Thermal Sciences*, 70, 41-53 (2013).
6. A. Ishak, Similarity solutions for flow and heat transfer over a permeable surface with convective boundary condition, *Appl. Math. Comput.* 217 (2010) 837-842.
7. A. Aziz, A similarity solution for laminar thermal boundary layer over a flat plate with a convective surface boundary condition, *Comm. Non. Sci. Num. Sim.* 14 (2009) 064-1068.
8. A. Aziz, Hydrodynamic and thermal slip flow boundary layers over a flat plate with constant heat flux boundary condition, *Comm. Non. Sci. Num. Sim.* 15 (2010) 573-580.
9. O.D. Makinde, P.O. Olanrewaju, Buoyancy effects on thermal boundary layer over a vertical plate with a convective surface boundary condition, *Trans. ASME J. Fluids Eng.* 132 (2010) 044502-2.
10. O.D. Makinde, A. Aziz, MHD mixed convection from a vertical plate embedded in a porous medium with a convective boundary condition, *Int. J. Therm. Sci.* 49 (2010) 1813-1820.
11. D. Gupta, L. Kumar, O Anwar Bég and B. Singh, Finite element simulation of mixed convection flow of micropolar fluid over a shrinking sheet with thermal radiation, *Proc. IMechE. Part E: J Process Mechanical Engineering* (2013). DOI: 10.1177/0954408912474586.
12. G. Swapna, Lokendra Kumar, O. Anwar Bég and Bani Singh, Effect of thermal radiation on the mixed convection flow of a magneto-micropolar fluid past a continuously moving plate with a convective surface boundary condition, *Meccanica* (2013). in press
13. O. D. Makinde, K. Zimba, O. Anwar Bég, Numerical study of chemically-reacting hydromagnetic boundary layer flow with Soret/Dufour effects and a convective surface boundary condition, *Int. J. Thermal and Environmental Engineering*, 4, 89-98 (2012).
14. O. Anwar Bég, M.J. Uddin, M.M. Rashidi and N. Kavyani, Double-diffusive radiative magnetic mixed convective slip flow with Biot number and Richardson number effects, *J. Engineering Thermophysics* (2013).
15. S.V. Subhashini, N. Samuel, I. Pop, Double-diffusive convection from a permeable vertical surface under convective boundary condition, *Int. Commun. Heat Mass Transfer* 38 (2011) 1183-1188.
16. R.E. Powell, H. Eyring, Mechanism for relaxation theory of viscosity, *Nature* 154 (1944) 427-428.
17. J. Zueco, O.A. Bég, Network numerical simulation applied to pulsatile non-Newtonian flow through a channel with couple stress and wall mass effects, *Int. J. Appl. Math. Mech.* 5 (2009) 1-16.
18. S. Islam, A. Shah, C.Y. Zhou, I. Ali, Homotopy perturbation analysis of slider bearing with Powell-Eyring fluid, *Z. Angew. Math. Phys.* 60 (2009) 1178-1193.
19. M. Patel, M.G. Timol, Numerical treatment of Powell-Eyring fluid flow using method of asymptotic boundary conditions, *Appl. Numer. Math.* 59 (2009) 2584-2592.
20. V. Sirohi, M.G. Timol, N.L. Kalathia, Numerical treatment of Powell-Eyring fluid flow past a 90 degree wedge, *Reg. J. Energy Heat Mass Transfer* 6 (3) (1984) 219-228.
21. N. S. Akbar, S. Nadeem, T. Hayat, A. A. Hendi, Simulation of heating scheme and chemical reactions on the peristaltic flow of an Eyring-Powell fluid, *Int. J. Numerical Methods for Heat & Fluid Flow*, 22, 764-776 (2012).
22. T. Hayat, Z. Iqbal, M. Qasim and S. Obaidat, Steady flow of an Eyring Powell fluid over a moving surface with convective boundary conditions, *Int. J. Heat and Mass Transfer*, 55, 1817 (2012).

23. D.Y. Etchart, A pipe entry length solution for heat transfer and flow in Powell-Eyring fluids with temperature-dependent viscosity and constant flux boundary, *PhD Thesis, Oregon State University, USA* (1971).
24. I.A. Hassanien and F.M. Hady, Hydromagnetic free convection and mass transfer flow of non-Newtonian fluid through a porous medium bounded by an infinite vertical limiting surface with constant suction, *Astrophysics and Space Science*, 116, 141-148 (1985).
25. V. Sirohi, M G Timol and N L Kalthia, Powell-Eyring model flow near an accelerated plate *Fluid Dyn.Res.*2, 193 (1987).
26. M. Yürüsoy, A Study of pressure distribution of a slider bearing lubricated with Powell-Eyring fluid, *Turkish J. Engineering Envir. Sciences*, 27, 299-304, (2003).
27. L. Ai and K. Vafai, An investigation of Stokes' second problem for non-Newtonian fluids, *Numerical Heat Transfer, Part A*, 47, 955-980 (2005).
28. O. Adesanya and J. A. Gbadeyan, Adomian decomposition approach to steady viscoelastic fluid flow with slip through a planer channel, *Int. J. Nonlinear Science*, 9, 86-94 (2010).
29. Eswara, A.T. and Nath G., Unsteady forced convection laminar boundary layer flow over a moving longitudinal cylinder. *Acta Mech.*, 93, 13-28 (1992).
30. Rotte, J. W. and Beek, W.J., Some models for the calculation of heat transfer coefficients to moving continuous cylinders. *Chem. Eng. Sci.*, 24, 705-716 (1969).
31. Sakiadis, B.C., Boundary behavior on continuous solid surfaces, III The boundary layer on a continuous cylindrical surface. *AIChE. J.*, 7: 467-472 (1961).
32. Zueco, J., O. Anwar Bég, Tasveer A. Bég and H.S. Takhar, Numerical study of chemically-reactive buoyancy-driven heat and mass transfer across a horizontal cylinder in a high-porosity non-Darcian regime, *J. Porous Media*,12, 519-535 (2009).
33. Zueco, J., O. Anwar Bég, H. S. Takhar and G. Nath, Network simulation of laminar convective heat and mass transfer over a vertical slender cylinder with uniform surface heat and mass flux, *J. Applied Fluid Mechanics*,4, 13-23 (2011).
34. Chen S.S. and Leonard R., The axisymmetrical boundary layer for a power-law non-Newtonian fluid on a slender cylinder, *Chem. Eng. J.*, 3, 88-92 (1972).
35. Lin, F. N. and Chern, S. Y., Laminar boundary-layerflow of non-Newtonian fluid, *Int. J. Heat Mass Transfer*, 22, 1323-1329 (1979).
36. Pop, I., Kumari, M. and Nath, G., Non-Newtonian boundary layers on a moving cylinder. *Int. J. Eng. Sci.*, 28, 303-312 (1990).
37. Chang, C.L., Buoyancy and wall conduction effects on forced convection of micropolar fluid flow along a vertical slender hollow circular cylinder, *Int. J. Heat Mass Transfer*, 49, 4932-4942 (2006).
38. Anwar, I., Amin, N. and Pop, I., Mixed convection boundary layer flow of a viscoelastic fluid over a horizontal circular cylinder, *Int. J. Non-Linear Mechanics*, 43, 814-821 (2008).
39. Kasim, A.R.M., Mohammad N.F. and S. Shafie, Effect of heat generation on free convection boundary layer flow of a viscoelastic fluid past a horizontal circular cylinder with constant surface heat flux, *5<sup>th</sup> Int. Conf. Research and Education in Mathematics (ICREM5), Bandung, Indonesia, 22-24 October* (2011).
40. Rehman, M.A. and Nadeem, S, Mixed convection heat transfer in micropolar nanofluid over a vertical slender cylinder, *Chin. Phys. Lett.*, 29, 124701 (2012).
41. Prasad, V.R., A. SubbaRao, N. Bhaskar Reddy, B. Vasu, O. Anwar Bég, Modelling laminar transport phenomena in a Casson rheological fluid from a horizontal circular cylinder with partial slip, *ProcIMEchE-Part E: J. Process Mechanical Engineering* (2012).
42. V. R. Prasad, B. Vasu, O. Anwar Bég and D. R. Parshad, Thermal radiation effects on magnetohydrodynamic free convection heat and mass transfer from a sphere in a variable porosity regime, *Comm. Nonlinear Science Numerical Simulation*, 17, 654-671 (2012).
43. K.A. Yih, Viscous and Joule Heating effects on non-Darcy MHD natural convection flow over a permeable sphere in porous media with internal heat generation, *International Communications in Heat and mass Transfer*, 27(4), 591-600 (2000).
44. H.B. Keller, Numerical methods in boundary-layer theory, *Ann. Rev. Fluid Mech.* 10, 417-433 (1978).
45. M. Subhas Abel, P.S. Datti, N. Mahesha, Flow and heat transfer in a power-law fluid over a stretching sheet with variable thermal conductivity and non-uniform heat source, *Int. J. Heat Mass Transfer* ,52, 2902-2913 (2009).
46. K. Vajravelu, K.V. Prasad, J. Lee, C. Lee, I. Pop and Rob. A. Van Gorder, Convective heat transfer in the flow of viscous Ag-water and Cu-water nanofluids over a stretching surface, *Int. J. Thermal Sciences*, 50, 843-851 (2011).
47. C-H. Chen, Magneto-hydrodynamic mixed convection of a power-law fluid past a stretching surface in the presence of thermal radiation and internal heat generation/absorption, *Int. J. Non-Linear Mechanics*, 44, 596-603 (2009).
48. Y.L. Zhang and K. Vairavamoorthy, Analysis of transient flow in pipelines with fluid-structure interaction using method of lines, *Int. J. Num. Meth. Eng*, 63, 1446-1460 (2005).
49. OrhanAydin and Ahmet Kaya, Non-Darcian forced convection flow of viscous dissipating fluid over a flat plate embedded in a porous medium, *Transport in Porous Media*, 73, 173-186 (2008).

50. M. Kumari, G. Nath, Steady mixed convection stagnation-point flow of upper convected Maxwell fluids with magnetic field, *Int. J. Nonlinear Mechanics*, 44, 1048-1055 (2009).
51. J.N. Potter and N Riley, Free convection from a heated sphere at large Grashof number, *J. Fluid Mechanics*, 100, 769-783 (1980).
52. A. Prhashanna, R.P. Chhabra, Free convection in power-law fluids from a heated sphere, *Chem. Eng. Sci.*, 65, 6190-6205 (2010).
53. H-T.Chen, C-K. Chen, Natural convection of a non-Newtonian fluid about a horizontal cylinder and a sphere in a porous medium, *Int. Comm. Heat Mass Transfer*, 15, 605–614 (1988).
54. O. Anwar Bég, D. Tripathi, J-L Curiel-Sosa and T-K Hung, Peristaltic propulsion of viscoplastic rheological materials, *Advances in Biological Modelling, Editor- T.Y. Wu, Taylor and Francis, Philadelphia, USA* (2014).
55. Merkin, J. H., “Free convection boundary layer on an isothermal horizontal cylinder”, ASME, paper no. 76-HT-16, (1976).
56. Nazar, R., Amin, N. and Pop, I., “Free convection boundary layer on an isothermal horizontal circular cylinder in a micropolar fluid” Heat transfer, Proceeding of the 12th int. conference (2002).

**TABLES**

**Table-1:** Values of  $C_f$  and  $Nu$  for different  $\varepsilon$  and  $Pr$  ( $\delta = 0.1, \gamma = 0.2, \xi = 1.0$ )

Pr	$\varepsilon = 0.0$		$\varepsilon = 0.3$		$\varepsilon = 0.5$		$\varepsilon = 0.7$	
	$C_f$	$Nu$	$C_f$	$Nu$	$C_f$	$Nu$	$C_f$	$Nu$
7	0.3501	0.3966	0.3789	0.3758	0.3954	0.3647	0.4103	0.3552
10	0.3261	0.4403	0.3523	0.4165	0.3674	0.4034	0.3809	0.3930
15	0.3000	0.4946	0.3236	0.4670	0.3371	0.4525	0.3492	0.4400
20	0.2823	0.5362	0.3041	0.5058	0.3166	0.4898	0.3279	0.4761
25	0.2690	0.5705	0.2896	0.5378	0.3014	0.5206	0.3121	0.5058
50	0.2308	0.6891	0.2476	0.6484	0.2578	0.6270	0.2666	0.6088
75	0.2105	0.7679	0.2259	0.7220	0.2347	0.6979	0.2427	0.6774
100	0.1970	0.8287	0.2113	0.7787	0.2194	0.7525	0.2268	0.7303

**Table-2:** Values of  $C_f$  and  $Nu$  for different  $\varepsilon$  and  $Pr$  ( $\delta = 0.1, \gamma = 0.2, \xi = 1.0$ )

Pr	$\varepsilon = 1.0$		$\varepsilon = 1.2$		$\varepsilon = 1.5$	
	$C_f$	$Nu$	$C_f$	$Nu$	$C_f$	$Nu$
7	0.4303	0.3430	0.4424	0.3360	0.4591	0.3267
10	0.3991	0.3792	0.4102	0.3713	0.4253	0.3608
15	0.3656	0.4242	0.3755	0.4151	0.3891	0.4032
20	0.3461	0.4588	0.3522	0.4488	0.3649	0.4358
25	0.3264	0.4872	0.3350	0.4766	0.3469	0.4626
50	0.2785	0.5859	0.2857	0.5728	0.2956	0.5557
75	0.2534	0.6517	0.2598	0.6370	0.2687	0.6177
100	0.2368	0.7024	0.2428	0.6864	0.2510	0.6655

**Table-3:** Values of  $C_f$  and  $Nu$  for different  $\delta$  and  $Pr$  ( $\varepsilon = 0.1, \gamma = 0.2, \xi = 1.0$ )

Pr	$\delta = 0.0$		$\delta = 5$		$\delta = 10$		$\delta = 15$	
	$C_f$	$Nu$	$C_f$	$Nu$	$C_f$	$Nu$	$C_f$	$Nu$
7	0.3604	0.3889	0.3598	0.3901	0.3592	0.3913	0.3592	0.3913
10	0.3354	0.4316	0.3350	0.4327	0.3345	0.4338	0.3340	0.4351
15	0.3084	0.4844	0.3080	0.4855	0.3077	0.4866	0.3073	0.4878
20	0.2901	0.5240	0.2898	0.5261	0.2895	0.5271	0.2892	0.5283
25	0.2764	0.5584	0.2761	0.5594	0.2759	0.5605	0.2756	0.5616
50	0.2369	0.6740	0.2368	0.6749	0.2366	0.6759	0.2365	0.6769
75	0.2160	0.7509	0.2159	0.7518	0.2158	0.7527	0.2156	0.7536
100	0.2021	0.8102	0.2020	0.8110	0.2019	0.8119	0.2018	0.8127

**Table-4:** Values of  $C_f$  and  $Nu$  for different  $\delta$  and  $Pr$  ( $\varepsilon = 0.1, \gamma = 0.2, \xi = 1.0$ )

Pr	$\delta = 20$		$\delta = 30$		$\delta = 40$	
	$C_f$	$Nu$	$C_f$	$Nu$	$C_f$	$Nu$
7	0.3579	0.3940	0.3567	0.3972	0.3557	0.4017
10	0.3336	0.4364	0.3326	0.4394	0.3328	0.4438
15	0.3070	0.4890	0.3063	0.4918	0.3056	0.4951
20	0.2889	0.5295	0.2883	0.5321	0.2878	0.5350
25	0.2754	0.5627	0.2749	0.5625	0.2744	0.5680
50	0.2363	0.6779	0.2361	0.6800	0.2358	0.6823
75	0.2155	0.7545	0.2153	0.7565	0.2151	0.7585
100	0.2017	0.8136	0.2016	0.8154	0.2014	0.8173

**Table-5:** Numerical Values of  $f''(\xi, 0)$  (in brackets) and skin friction coefficient  $C_f$  for different values of  $\delta$  and  $\varepsilon$

$\delta \setminus \varepsilon$	0.0	0.2	0.4	0.6	0.8	1.0
0.0	0.3501	0.3699 (0.3083)	0.3874 (0.2767)	0.4031 (0.2519)	0.4173 (0.2318)	0.4304 (0.2152)
0.1	0.3501	0.3699 (0.3084)	0.3874 (0.2769)	0.4031 (0.2521)	0.4173 (0.2320)	0.4303 (0.2153)
0.2	0.3501	0.3699 (0.3086)	0.3873 (0.2771)	0.4030 (0.2523)	0.4172 (0.2322)	0.4303 (0.2155)
0.3	0.3501	0.3699 (0.3087)	0.3873 (0.2773)	0.4030 (0.2525)	0.4172 (0.2323)	0.4303 (0.2156)
0.4	0.3501	0.3699 (0.3089)	0.3873 (0.2775)	0.4029 (0.2526)	0.4172 (0.2325)	0.4302 (0.2158)
0.5	0.3501	0.3699 (0.3090)	0.3873 (0.2776)	0.4029 (0.2528)	0.4171 (0.2327)	0.4302 (0.2159)
0.6	0.3501	0.3698 (0.3092)	0.3872 (0.2778)	0.4029 (0.2530)	0.4171 (0.2328)	0.4302 (0.2161)
0.7	0.3501	0.3698 (0.3093)	0.3872 (0.2780)	0.4028 (0.2532)	0.4170 (0.2330)	0.4301 (0.2163)
0.8	0.3501	0.3698 (0.3095)	0.3872 (0.2782)	0.4028 (0.2536)	0.4170 (0.2332)	0.4301 (0.2164)
0.9	0.3501	0.3698 (0.3096)	0.3872 (0.2784)	0.4028 (0.2536)	0.4170 (0.2334)	0.4300 (0.2166)
1.0	0.3501	0.3697 (0.3098)	0.3871 (0.2786)	0.4028 (0.2538)	0.4170 (0.2335)	0.4300 (0.2167)

**COMPARISON TABLE:** In order to verify the accuracy of our present method, we have compared our results with those of Merkin [49] and Nazar *et al.* [50]. The present results are found to be in good agreement.

$$Nu Gr^{-1/4} = -\theta'(\xi, 0)$$

$\xi$	Merkin[55]	Nazar et. al.[56]	Present
0	0.4214	0.4214	0.4215
$\pi/6$	0.4161	0.4161	0.4162
$\pi/3$	0.4007	0.4005	0.4006
$\pi/2$	0.3745	0.3741	0.3742
$2\pi/3$	0.3364	0.3355	0.3357
$5\pi/6$	0.2825	0.2811	0.2821
$\pi$	0.1945	0.1916	0.1935

FIGURES

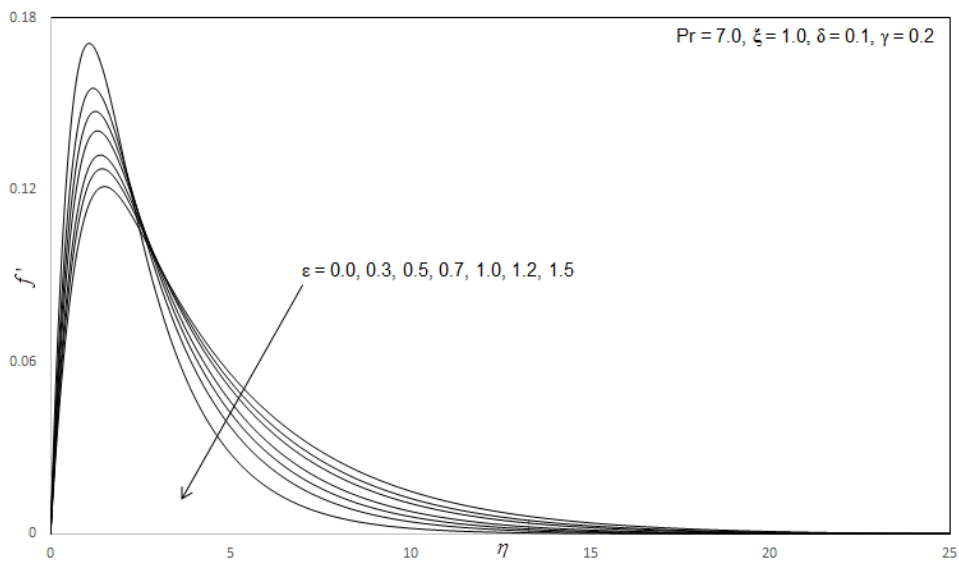


Fig. 3(a) Effect of  $\epsilon$  on the Velocity Profiles

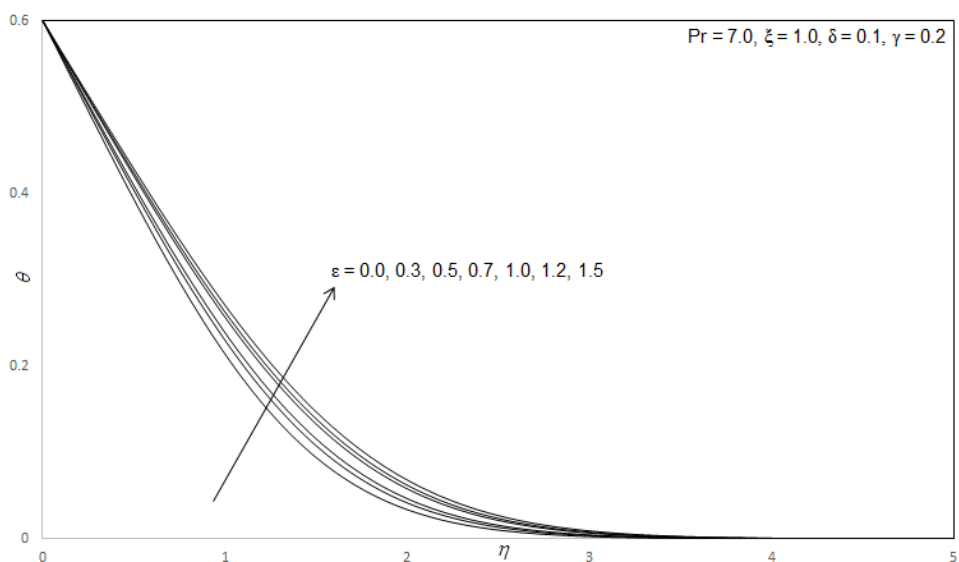


Fig. 3(b) Effect of  $\epsilon$  on the Temperature Profiles

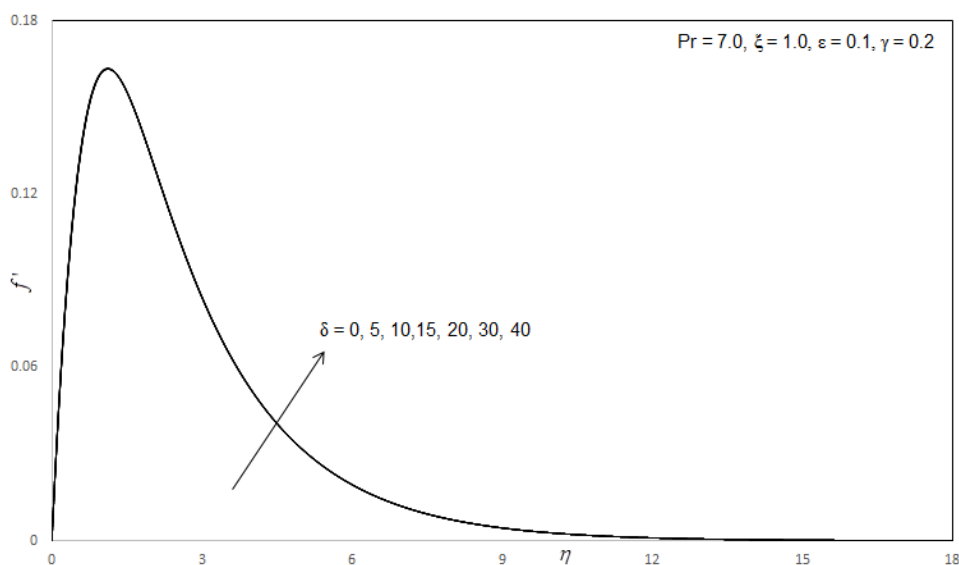


Fig. 4(a) Effect of  $\delta$  on the Velocity Profiles

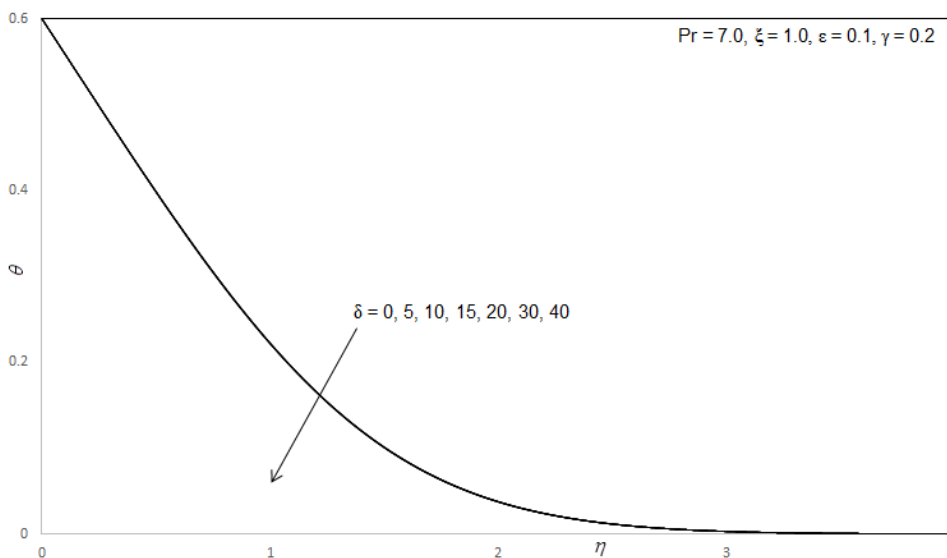


Fig. 4(b) Effect of  $\delta$  on the Temperature Profiles

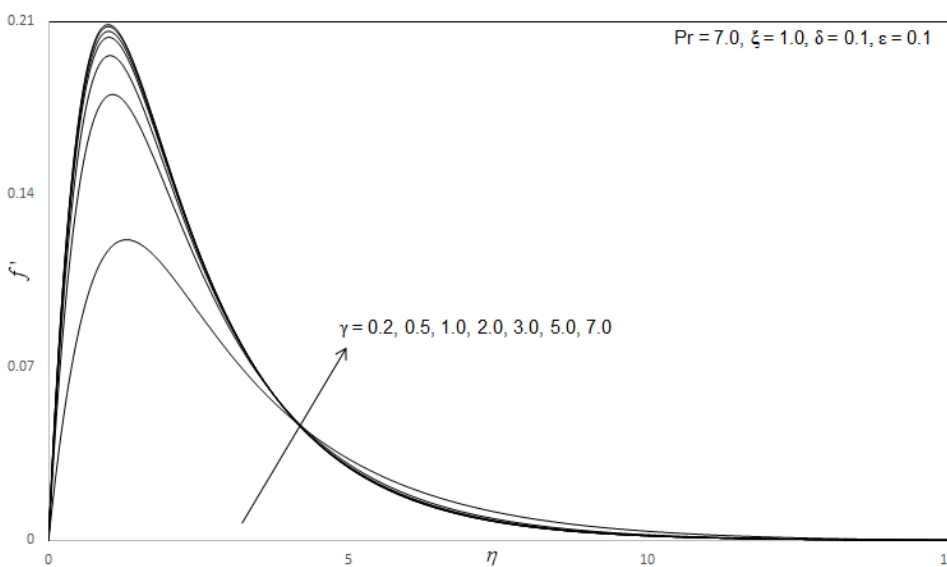


Fig. 5(a) Effect of  $\gamma$  on the Velocity Profiles

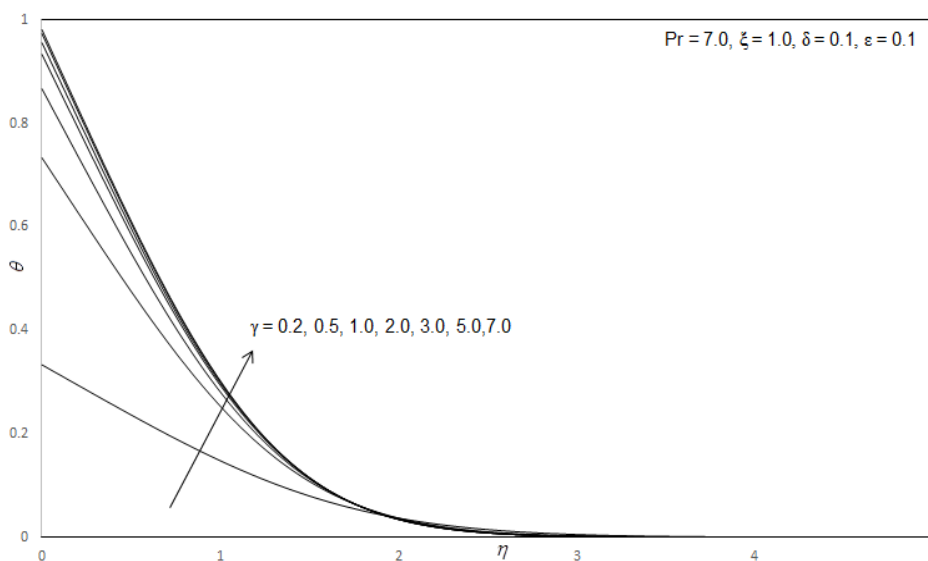


Fig. 5(b) Effect of  $\gamma$  on the Temperature Profiles

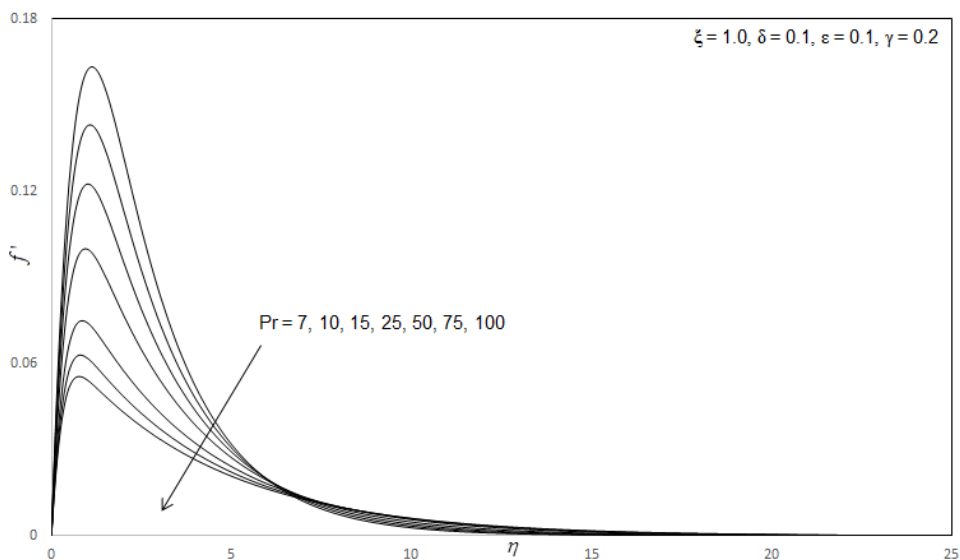


Fig. 6(a) Effect of Pr on the Velocity Profiles

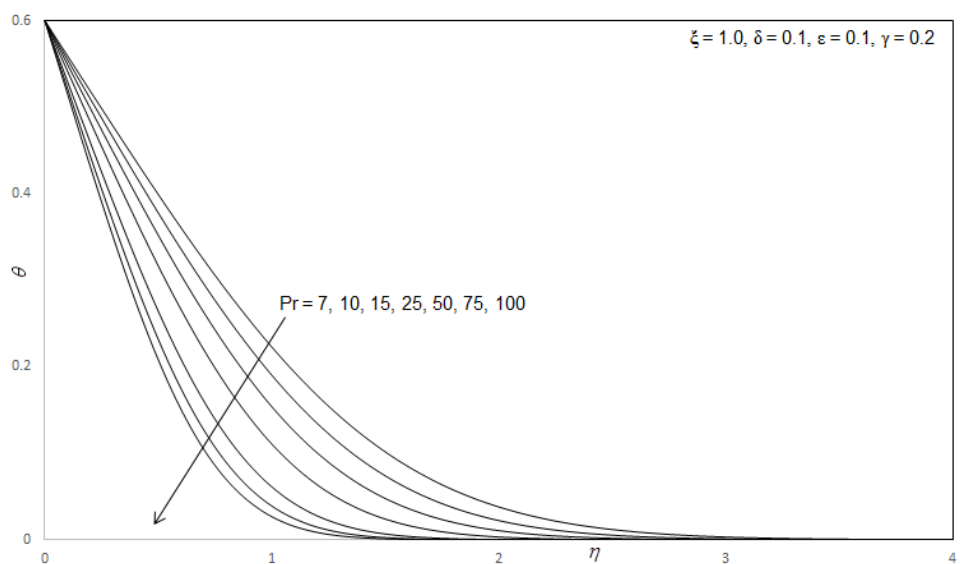


Fig. 6(b) Effect of Pr on the Temperature Profiles

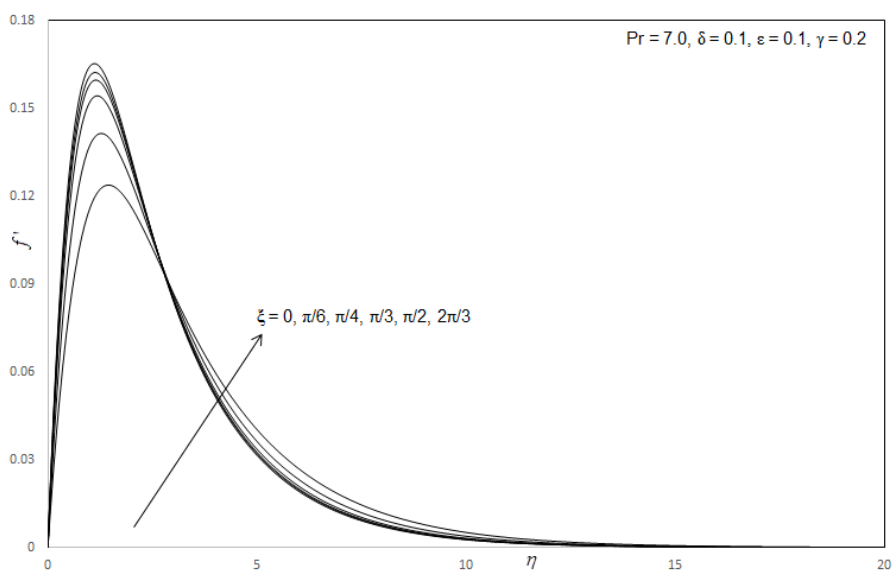


Fig. 7(a) Effect of  $\xi$  on the Velocity Profiles



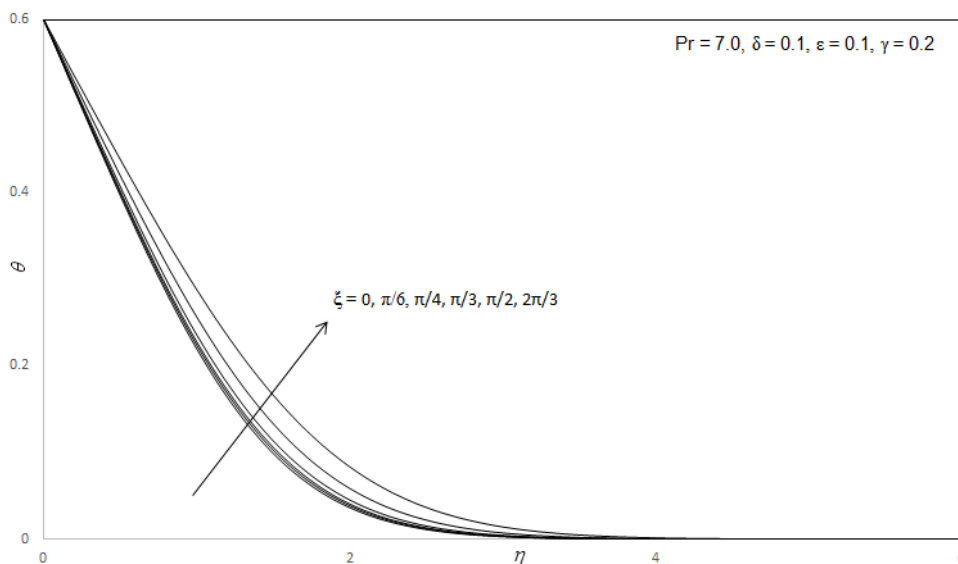


Fig. 7(b) Effect of  $\xi$  on the Temperature Profiles

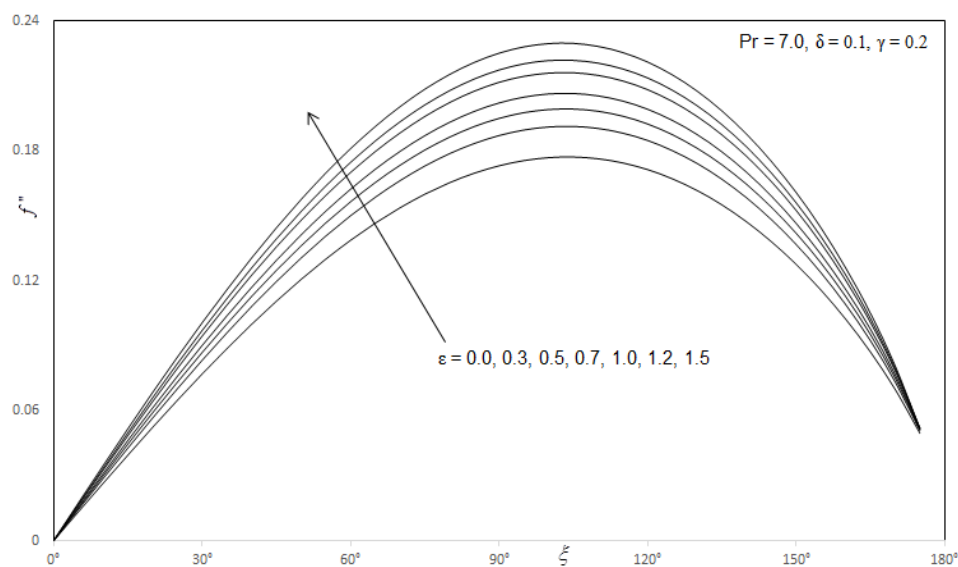


Fig. 8(a) Effect of  $\epsilon$  the Skin Friction

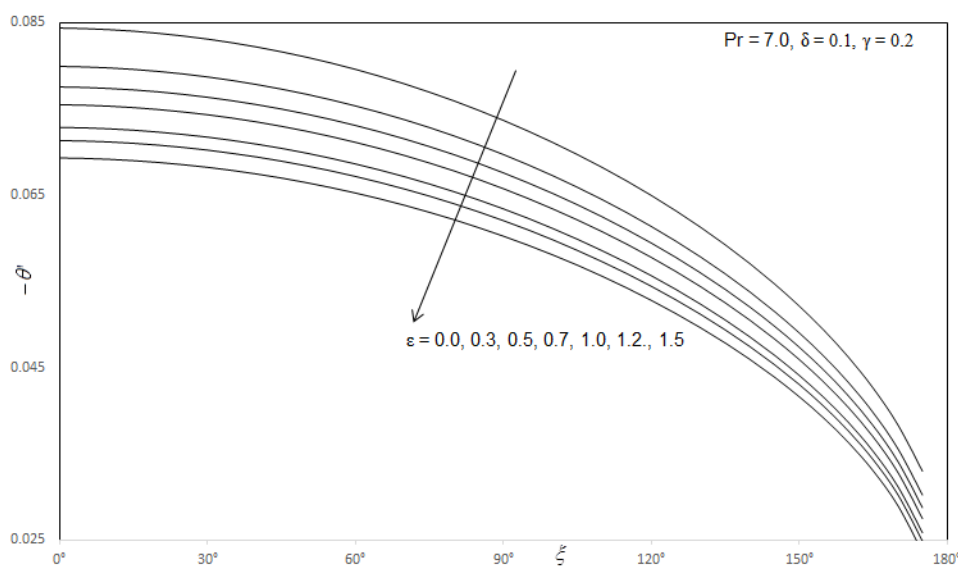


Fig.8(b) Effect of  $\epsilon$  on the Local Nusselt Number

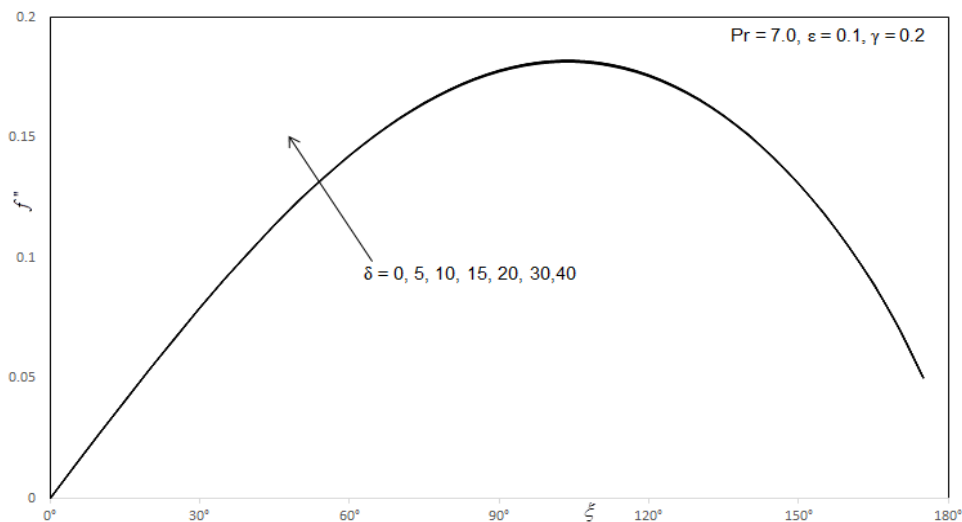


Fig. 9(a) Effect of  $\delta$  on the Skin Friction

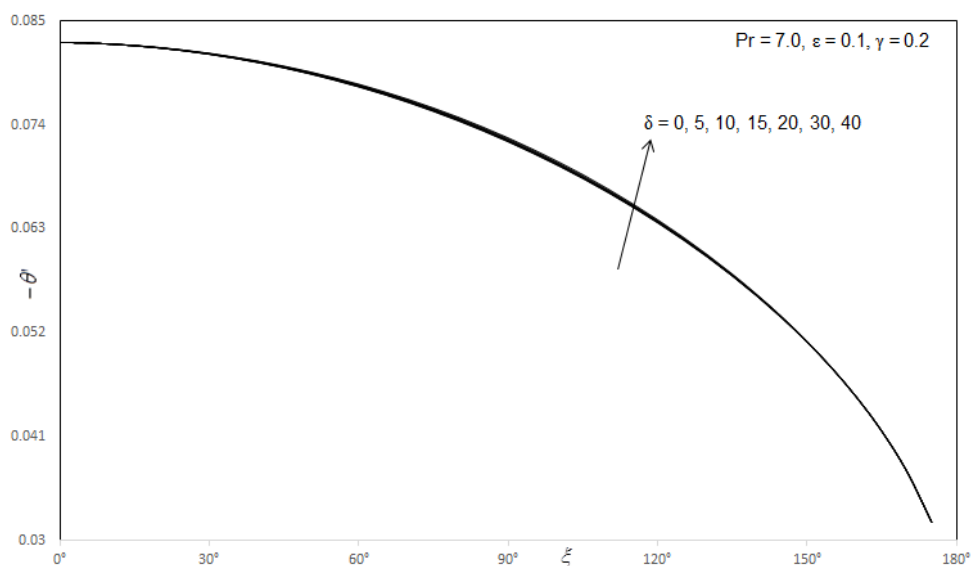


Fig. 9(b) Effect of  $\delta$  on the Local Nusselt Number

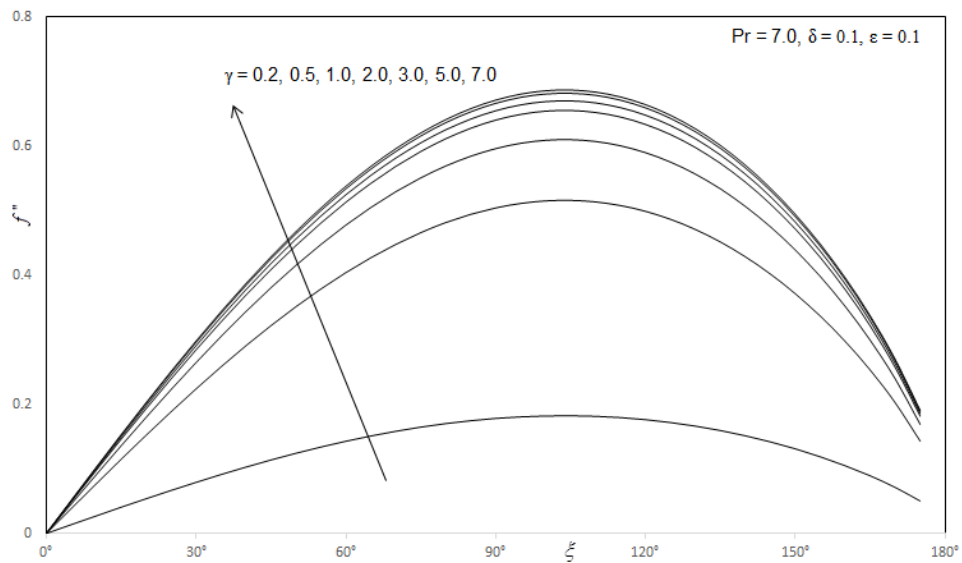


Fig. 10(a) Effect of  $\gamma$  on the Skin Friction

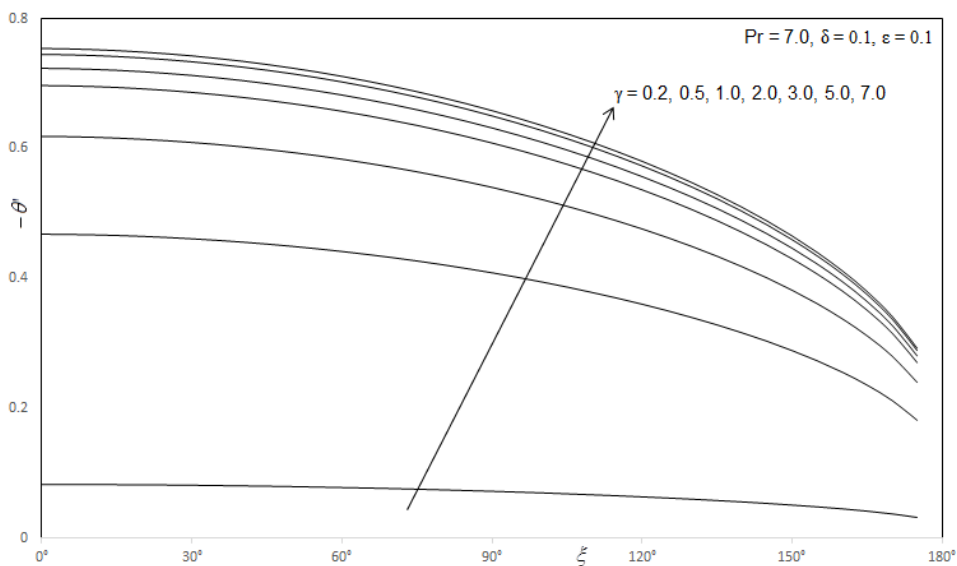


Fig. 10(b) Effect of  $\gamma$  on the Local Nusselt Number

**Source of support: Nil, Conflict of interest: None Declared**

**[Copy right © 2015. This is an Open Access article distributed under the terms of the International Journal of Mathematical Archive (IJMA), which permits unrestricted use, distribution, and reproduction in any medium, provided the original work is properly cited.]**